Defects at the Si(001)/a-SiO_2 interface: Analysis of structures generated with classical force fields and density functional theory

E. Mehes and C. H. Patterson
School of Physics, Trinity College Dublin, Dublin 2, Ireland
(Received 6 April 2017; revised manuscript received 1 August 2017; published 29 September 2017)

Defects at the Si(001)/a-SiO_2 interface were simulated using a combination of classical force field molecular dynamics and first-principles total-energy minimization techniques. The second generation charge-optimized many-body potential COMB10 was used to generate a-SiO_2 which was placed on an ideally terminated Si(001) surface and briefly annealed before being relaxed using density functional theory. Si dimers form at the Si interface on relaxation unless the Si surface has been oxidized. P_{b1} defects form when Si dimers do not bond to O atoms in the a-SiO_2 layer. Mismatch in Si atom pairings at the dimerized surface leads to $Si_2O{\equiv}Si\cdot$ defects at the interface which may be the structure of a defect denoted S in electron-spin resonance (ESR) studies. Relatively few P_{b0} defects with a magnetic moment form at the Si interface. a-SiO_2 generated by heating and quenching a system with periodic boundary conditions is free of E' defects. Afterward, this structure is placed on the Si surface and allowed to relax. The main type of E' defect which forms is a forward oriented E'_α defect. ESR hyperfine parameters for each defect category are calculated and compared to experimental data. Defect densities of states are calculated and compared to experiment.

DOI: 10.1103/PhysRevMaterials.1.044602

I. INTRODUCTION

Defects at semiconductor/oxide interfaces in metal-oxide-semiconductor field-effect transistor (MOSFET) devices are commonly characterized as interface states or oxide traps, depending on their character and localization at the interface or deeper in the oxide layer [1,2]. States at Si/amorphous SiO_2 (a-SiO_2) interfaces, observed via electron-spin resonance (ESR), are predominantly Si dangling bonds (DBs) and are referred to as P_b defects [3–7]; other interface states have been labeled P_m [8] and S [9]. The P_{b0} defect has been assigned to Si DBs with [111] orientations at the Si/a-SiO_2 interface, and the P_{b1} defect has been assigned to Si dimers at the interface with one DB [4]. Positions of charge transition levels with respect to the Fermi level for P_{b1} defects at the Si(100)/a-SiO_2 interface have been controversial [10–12] and, more recently, there have been several attempts to measure the density of states (DOS) for P_b and other interface states at the Si(001)/a-SiO_2 interface [13–15]

Here we present results of a study in which SiO_2 was amorphized using the second generation charge-optimized many-body potential (COMB10) classical force field (CFF) [16] before being placed onto a Si slab with a (001) surface orientation and relaxed using COMB10. The resulting Si/a-SiO_2 layered structure was relaxed further using a density functional theory (DFT) method. Finally, defect densities of states were calculated in the valence and Si $2p$ energy regions using a hybrid DFT method, which was adjusted so that the experimental bulk Si band gap is predicted correctly. The emphasis of this paper is on validating this approach by analyzing predicted properties of P_b interface defects and E' bulk a-SiO_2 defects and comparing predictions of the model to available experimental data. In particular, hyperfine Hamiltonian parameters are calculated and compared to parameters from ESR data and the defect density of states is compared to data from ESR [13], deep level transient spectroscopy (DLTS) [14], and charge pumping [15] experiments.

Modeling systems such as Si/SiO_2 interfaces presents challenges: structure information at the interface is limited [17–21]; extensive *ab initio* molecular dynamics (AIMD) simulations are expensive; predictions of structure based on the CFF for this interface have been tested to a limited extent [16,22–24]. The a-SiO_2/Si interface has been characterized by various experimental techniques: Rutherford ion scattering [21] and grazing incidence x-ray photoelectron spectroscopy [17,20] measurements have been used to characterize the a-SiO_2/Si interface at the atomic scale. The Si/a-SiO_2 interface structure employed in computer simulation studies thus far has mostly been generated using CFF or AIMD techniques [16,23–25], using DFT total-energy minimization techniques [26–30], or using a combination of these techniques [21,31–33]. Some of these simulations generated interface structures which had no O vacancy defects or Si DB at the interface [25,27,31,32]. Where vacancies and/or DB defects were created, it was done by selectively removing atoms [26] or by inserting extra O atoms in Si-Si bonds [28,29] or in a CFF-MD run [24]. Recent work by Kovačević and Pivac [24] used the ReaxFF [34] to simulate various a-SiO_2/Si interfaces with no subsequent DFT relaxation of the structure.

Two Si(001) surface terminations were used in this paper. The first is an ideal (undimerized) Si(001) clean surface termination and the second has 0.5 monolayers (MLs) of O atoms inserted within alternating rows of top layer Si atoms to form O bridges between Si atoms [35]. This is intended to mimic insertion of O into Si dimers in the initial stages of oxidation of a clean Si(001) surface. Hereafter, the ideal Si surface termination is referred to as unoxidized and the latter is referred to as oxidized. There are important differences between interface structures predicted by CFF-MD and the structure obtained after DFT total-energy minimization for the unoxidized surfaces. In particular, Si dimers form extensively at the unoxidized interface only after the DFT relaxation step. The COMB10 CFF does not predict formation of dimers. This is more likely to be a shortcoming of the CFF rather than the

 ©2017 American Physical Society

DFT Perdew-Burke-Ernzerhof (PBE) functional. DBs at these dimers result in P_{b1} defects which have been identified using ESR [4]. Beginning with an unoxidized, ideal Si(001)-(2 × 2) surface termination, top layer Si atoms have to displace in a correlated way in order to form Si dimers. Incomplete dimerization occurs when the a-SiO_2 layer is placed on top of Si and some dimer "mismatches" occur in which one of the Si dimer atoms is left without a partner. This results in Si DBs oriented parallel to the interface and formation of $Si_2O{\equiv}Si\cdot$ defects. These may be the S defect observed in fused silica glasses [36], and after high-temperature annealing of the Si(001)/a-SiO_2 interface [9].

Oxygen vacancy defects in bulk c-SiO_2 and a-SiO_2 silica produce Si DB states known as E' centers. Charge traps in devices with a-SiO_2/Si interfaces and large charging time constants are likely to be E' defects in the gate oxide layer. Defects denoted E'_α [37–39], E'_β [37], E'_γ [40–43], and E'_δ [37,44,45] have been identified in a-SiO_2 and nanometer sized silica particles [46] by ESR, which are distinguished by their hyperfine splitting.

The remainder of this paper is organized as follows: methods used for generating the Si/a-SiO_2 interface are described and the predicted properties of bulk a-SiO_2 and the Si/a-SiO_2 interface are compared to available experimental data; defect densities of states and ESR hyperfine parameters are presented and compared to experimental data; the discussion focuses on comparison of ESR parameters from this paper and experiment and the suitability of the method used here for generating semiconductor/oxide interfaces.

II. METHODOLOGY

The Si(001)/a-SiO_2 interface structure was generated using CFF-MD with the COMB10 force field [16] in the LAMMPS code [47,48] and total-energy minimization calculations using the PBE DFT functional [49] in the CASTEP code [50]. Since DFT generally underestimates electronic band gaps, electronic wave functions, energy eigenvalues, and ESR hyperfine tensors were calculated using a modified version [51] of the B3LYP hybrid DFT functional in the CRYSTAL code [52]. The electronic DOS was calculated using these hybrid DFT wave functions and eigenvalues and a tetrahedron method in the EXCITON code [53].

A. α quartz and a-SiO_2

Atomic positions and lattice parameters for α quartz were obtained using a modified B3LYP hybrid DFT functional in the CRYSTAL code. The weight of Fock exchange in the B3LYP functional was adjusted to 5%. This modified functional correctly predicts the band gap of bulk c-Si [51]. A larger weight of Fock exchange would be needed to produce an α quartz band gap in agreement with experiment. However, correct prediction of the Si band gap is more important in this paper as defect levels relative to Si band edges are needed. The predicted mass density was 2.30 g cm^{-3}, which is somewhat less than the experimental value of 2.65 g cm^{-3}. Predicted Si-O bond lengths are 1.626 and 1.617 Å and are in good agreement with the experimental value of 1.61 Å [54]. Band gaps for α quartz and a-SiO_2 are predicted to be 6.3 and 6.1 eV,

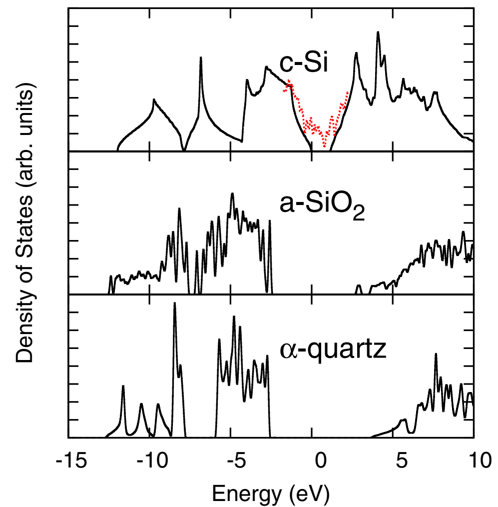

FIG. 1. Density of states for c-Si, a-SiO_2, and α quartz from hybrid DFT calculations. The average valence DOS for six Si/a-SiO_2 unit cells around the Fermi level is shown as a dotted line in the top panel.

respectively, which underestimate experimental values of 9.7 [55] and 9.3 eV [56].

a-SiO_2 supercells containing 84 ions with the experimental mass density of 2.20 g cm^{-3} were generated from COMB10 CFF-MD LAMMPS runs beginning from an α quartz supercell. After an equilibration period at high temperature, the dynamics was quenched by reducing the temperature from 5000 to 200 K at 500 K ps^{-1}. Quenches of this type, beginning at temperatures ranging from 3000 to 5500 K in steps of 500 K and lasting 10 ps, were tested for generation of a-SiO_2 supercells. Quenches beginning at 5000 K were judged to give the best structures (in that they did not resemble the initial α quartz supercell and had few broken Si-O bonds). We note that the dependence of a-SiO_2 structure on quench rate in the range from 8 to 1140 K ps^{-1} was studied previously [57]. A quench rate of 100 K ps^{-1} was used to generate a-SiO_2 in recent work on the Si(001)/a-SiO_2 interface [33]. A Nosé-Hoover thermostat in the particle number, pressure and temperature (NPT) ensemble was used throughout the CFF-MD runs. Structures were subsequently relaxed using the PBE DFT functional in the CASTEP code. The modified B3LYP functional in the CRYSTAL code was used to obtain the electronic DOS of these relaxed structures. The DOS of one of these structures is compared to that of α quartz in Fig. 1. The atomic structure and radial distribution function for this case are shown in Figs. 2 and 3 of Ref. [58].

B. Si(001)/a-SiO_2 interfaces

Si/a-SiO_2 supercells were created by placing a Si slab containing 64 Si atoms with a (001) surface in contact with an 84 atom a-SiO_2 structure, generated as described in Sec. II A, to yield 148 atom cells (Fig. 2). Three 148 atom supercells of this kind were generated, with no modification of the interface by oxidation, and are denoted "unoxidized." A further three supercells were generated in which 0.5 ML of oxygen atoms were introduced in dimer bridges in the Si(001) surface. These

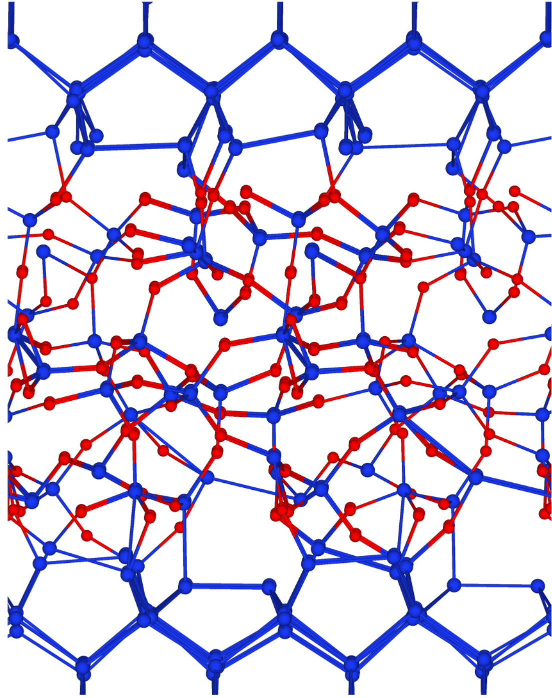

FIG. 2. Unoxidized Si(001)/a-SiO_2 interface supercell structure with 148 atoms. The view shown is along a dimer row direction and Si dimer bonds can be clearly seen at both interfaces. Two unit cells are shown side by side. Si ions, blue spheres; O ions, smaller red spheres.

cells contained a further eight O atoms and 156 atoms in total. Atomic positions in these interface supercells were initially relaxed using COMB10 and subsequently atomic positions and lattice parameters were relaxed using spin-polarized PBE DFT in CASTEP. Angles between lattice vectors were constrained to be 90° during structure relaxation using PBE DFT.

Equilibrium lattice parameters of the 84 atom a-SiO_2 cell were 10.47, 10.89, and 10.88 Å using PBE DFT, averaging to 10.73 Å. The equilibrium lattice parameter for crystalline Si (c-Si) using PBE DFT was 5.42 Å. The Si layer was a 2×2 supercell of the bulk conventional cell of the diamond structure, so that the equilibrium c-Si lattice constant parallel to the Si surface was 10.84 Å. Equilibrium lattice parameters for supercells containing Si(001)/a-SiO_2 interfaces averaged 10.73 Å and ranged from 10.18 to 11.09 Å. The unit-cell areas parallel to the interface ranged from 96.1 to 100.2% of the PBE DFT equilibrium values, with an average value of 98.3%. The Si layer is therefore under compressive strain in most of the six supercells used. Si layers in the real system are expected to be close to their equilibrium lattice constant close to the interface. It is not known how the strain in our simulations affects the defect density of states, etc. The supercells used do sample an ensemble of in-plane Si strains and we expect that it is important to allow a full relaxation of the supercell lattice parameters.

C. ESR hyperfine parameters

ESR spectra of Si DB defects can be explained by Zeeman and hyperfine Hamiltonians:

$$H = \mu_B \mathbf{B}.\mathbf{g}.\mathbf{S} + \mathbf{I}.\mathbf{A}.\mathbf{S}. \quad (1)$$

B is the external magnetic field, **g** is the electron g tensor (with values taken from ESR experiment), **I** is the nuclear spin of ^{29}Si nuclei (which have a 5% natural abundance), and **S** is the electron-spin operator. The coupling constant **A** contains an isotropic Fermi contact term,

$$\mathbf{A}_0 = \frac{2\mu_0}{3} g\beta_e g_n \beta_n \rho_{\text{spin}}(0)\mathbf{1}, \quad (2)$$

and an anisotropic term describing dipolar coupling between ^{29}Si nuclei and the electron spin on the primary defect site:

$$\mathbf{A}_1 = \frac{\mu_0}{4\pi} g\beta_e g_n \beta_n \mathbf{T}, \quad (3)$$

where **1** is the 3×3 unit matrix and **T** is a traceless, symmetric 3×3 tensor:

$$(\mathbf{T})_{ij} = \sum_{\mu\nu\sigma} P_{\mu\nu\sigma} \int d\mathbf{r}\, \phi_{\mu\sigma}(\mathbf{r}) \left(\frac{r^2\delta_{ij} - 3x_i x_j}{r^5} \right) \phi_{\nu\sigma}(\mathbf{r}). \quad (4)$$

g and g_n are the free-electron and nuclear g factors. β_e and β_n are the Bohr and nuclear magnetons and $\rho_{\text{spin}}(0)$ is the electron-spin density at the nucleus. **T** tensors [59] in this paper are calculated using the full spin-polarized density matrix, $P_{\mu\nu\sigma}$, and Bloch basis functions, $\phi_{\mu\sigma}$. σ is an occupied state electron spin. When the hyperfine tensor is axially symmetric, it can be completely specified by two parameters, a and b, where $A_\parallel = a + 2b$ and $A_\perp = a - b$. a is equal to the Fermi contact term magnitude, A_0.

III. RESULTS

A. Si(001)/a-SiO_2 interface structure

In this section we compare defect densities in supercells described above to densities obtained from experimental estimates. We also compare the Si $2p$ DOS from these supercells to photoemission data. The number of P_b defects at the Si(001)/a-SiO_2 interface has been estimated using ESR intensities [5], DLTS measurements [14], and capacitance-voltage curves in charge pumping (CP) experiments [15]. The P_{b1} density was found to be in the range 1 to 6×10^{12} cm^{-2}, depending on annealing temperature [5]. CP measurements on high-quality MOSFETs with 5.5-nm SiO_2 gate dielectrics yielded an estimate of 5×10^{10} cm^{-2} eV^{-1} P_b defects [15] and an energy integrated density of around 2×10^{10}cm^{-2}. DLTS measurements on MOS capacitors [14] found a maximum P_b density of 2.8×10^{12}cm^{-2} eV^{-1} and an energy integrated density around 3×10^{11} cm^{-2}. In calculations presented here, there are between two and six P_b defects per cell, each of which has two Si/a-SiO_2 interfaces and an area of 1.1×10^{-14} cm^2, yielding P_b defect densities in the range 10^{14} cm^{-2}, about 100 times higher than the defect densities measured by ESR [5,60]. The P_{b1} defect density in our calculations is determined by the structure which results from placing the a-SiO_2 from a CFF-MD run on top of the Si layer and the way in which dimers form when the supercell is allowed to relax using the PBE density functional. Structures of all six supercells used to model the interface structure (with oxidized or unoxidized Si layers) are shown in Fig. 1 of Ref. [58]. Passivation by annealing in H_2 and similar treatments reduce the defect density in experimental measurements. In this paper it was

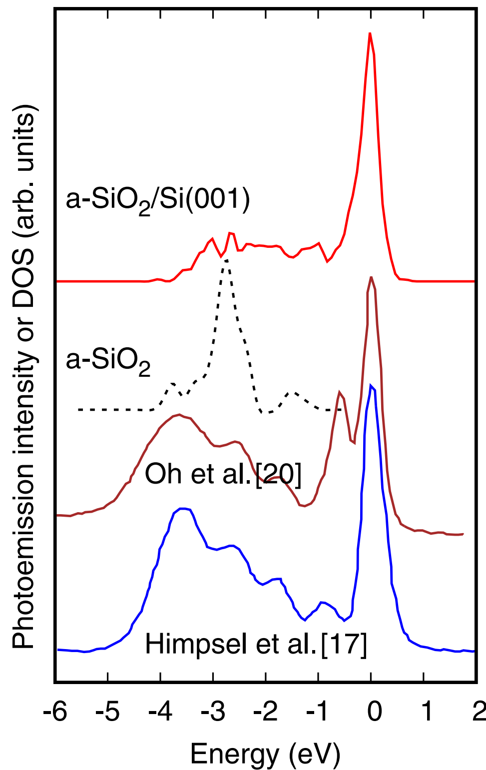

FIG. 3. Photoemission intensity vs binding energy relative to the bulk Si $2p_{3/2}$ binding energy and density of Si $2p$ states from DFT calculations on Si(001)/a-SiO_2 slabs and a-SiO_2. Photoemission data were redrawn from Figs. 4 and 1(a) in Refs. [17,20], respectively.

found that adding H to P_b defects eliminated defect DOS from the band gap, as might be expected.

The number density of E' spins in an ESR experiment is typically 10^{16} to 10^{17} cm^{-3} [6,39,40]. The number density of E' defects generated in this paper is of the order of 10^{21} cm^{-3}. For both interface and bulk a-SiO_2 defects, the linear density is about ten times higher than in experiments.

Angle resolved Si $2p$ core level spectroscopy has been used extensively to probe thin oxide layers on Si crystal surfaces. Five oxidation states are observed (Si^0 to Si^{IV}) and these are assumed to belong to Si bonded to up to four O atoms on going from bulk Si to the a-SiO_2 layer. These experiments therefore yield information on the structure and thickness of the interface layer. Si^I to Si^{IV} oxidation states have chemical shifts up to 4 eV to higher binding energy from the bulk Si $2p$ photoemission peak [17,20]. The clean, dimerized (2×1) Si(001) surface has a peak shifted to lower binding energy by 0.5 eV [17]. By measuring intensities of the various oxidation states as a function of polar emission angle it is possible to estimate the relative abundance of these oxidation states and their nearness to the surface in a thin a-SiO_2 film grown on Si(001). Himpsel *et al.* estimated that there is an equivalent of 1.9 ML of Si^{2+} and Si^{3+} at the Si(001) interface and found that the ratio of Si^{n+} is 1.10:0.48:0.28:0.24 for $n = 0$ to 3 with an incident photon energy of 400 keV [17]. Note that finite escape depths from thin oxide films on Si mean that the Si^{IV} signal in the oxide layer will be enhanced relative to the buried, bulk Si^0 signal. This is not the case for the computed spectra in Fig. 3.

In Fig. 3 we show the Si $2p$ DOS averaged over all six oxidized and unoxidized slabs used in this paper. These six cells contain 672 Si atoms in total. We also show the Si $2p$ DOS for the 84 atom a-SiO_2 unit cell illustrated in Fig. 2 of Ref. [58], which contains 28 Si atoms. Figure 3 also shows data redrawn from the work of Himpsel *et al.* [17] and Oh *et al.* [20]. This shows Si $2p_{3/2}$ levels of thin oxide films on Si(001). Five distinct oxidation states for Si are resolved in both cases. Maxima of the Si^0 peaks have been aligned for the interface supercell calculation and the two experimental curves. The same energy shift was applied to the a-SiO_2 DOS and the interface. The computed DOS range of energy shift relative to bulk Si is smaller than in experiment, possibly because final-state relaxation effects are omitted from the DFT calculations. The distinct oxidation states which are evident in experiment are not resolved in the DFT DOS calculation. The number of Si ions in the oxide layer in any oxidation state is relatively small. Mapping any limited range of DOS outside the main Si^0 peak onto sites in the slab did not show layerwise localization. The highest binding energy sites are E' defect sites in the a-SiO_2 layer. Interface Si dimer DOSs are shifted to slightly lower binding energy than the main Si^0 peak but this is not clearly resolved in the plot. Oh *et al.* found that their data for ultrathin a-SiO_2 layers on Si(001) [20] showed a line labeled α with a chemical shift of -0.25 eV relative to the bulk Si $2p$ line, which may be interface Si dimers.

B. P_{b0} and P_{b1} defects

Models for defects at Si/a-SiO_2 interfaces recognize two types of $Si_3{\equiv}Si\cdot$ defect: P_{b0} and P_{b1}. The former is a Si DB on an Si atom bonded to three Si atoms in the Si surface layer. Since it is located at the Si surface, the axis of the DB is expected to have one of four possible [111] orientations [4,6]. The latter has been assigned to a Si DB on a Si dimer at the interface and the hyperfine principal axis lies approximately along a [211] direction [4]. Hyperfine couplings of P_b defects to ^{29}Si nuclei have approximately axial symmetry [4].

Three P_{b0} defects with large magnetic moments on the Si DB atom were found at the 12 interfaces generated. Others were in a charged state with small magnetic moments. The spin density from one of these defects is shown in Fig. 4(a) and the atom projected density of states for these defects is shown in Fig. 5. The atom projected majority-spin density of states for these defects shows that the occupied states are closest to the Fermi level of all the spin-polarized defects found. These defects also have the least exchange splitting.

Hyperfine parameters for P_{b0} defects are given in Table I. The column labeled "Moment" gives the degree of localization of the magnetic moment on one defect DB site. The column labeled "Axis" gives the angle between the [111] direction and the hyperfine tensor principal axis. The Fermi contact hyperfine parameter for the three P_{b0} defects ranges from 1.9 to 9.2 mT. The hyperfine splitting of the ESR resonance which is generally assigned to the P_{b0} defect ranges from 10.0 to 10.7 [3]. Two of the defects have hyperfine tensor principal axes which lie close to a [111] axis and one is inclined at 38° to the nearest [111] axis. In each case the hyperfine tensor is nearly perfectly axial.

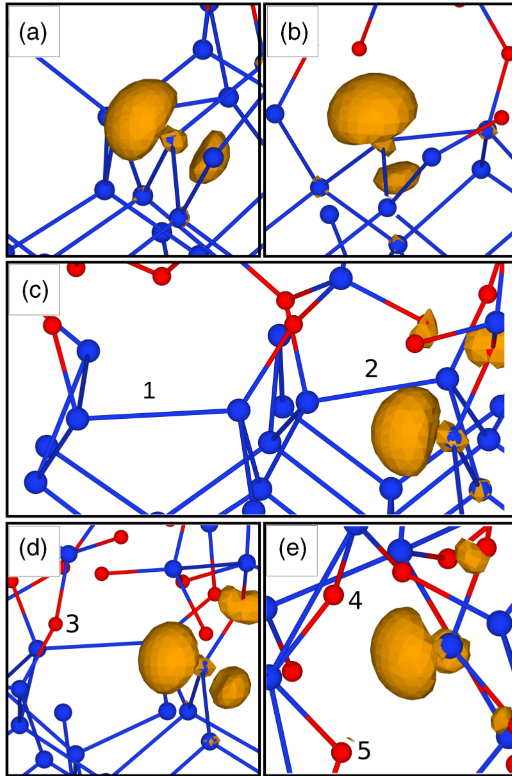

FIG. 4. Spin density for (a) P_{b0} defect 1, (b) P_{b1} defect 1, (c) $Si_2O{\equiv}Si\cdot$ defect 3 and dimers 1 and 2, (d) $Si_2O{\equiv}Si\cdot$ defect 1 and O ion 3, and (e) E'_α defect 2 and O ions 4 and 5. Numbered defects refer to defect labels in Tables I–IV. The $Si_2O{\equiv}Si\cdot$ DB in panel (c) is directed towards Si dimer 1 and is in the same row as dimer 2. The $Si_2O{\equiv}Si\cdot$ DB in panel (d) is directed towards O ion 3 and the E'_α DB is directed towards O ions 4 and 5.

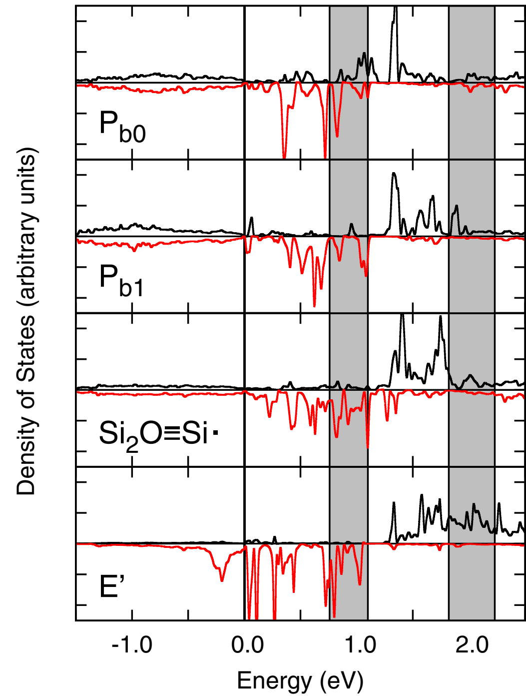

FIG. 5. Atom projected densities of states for Si atoms with largest magnetic moments. Densities of states are projected onto Si DB atoms in all six supercells used in this paper. The Si layer valence-band maximum is located at 0.0 eV and ranges of Fermi levels and conduction-band minima for the six cells are indicated by gray rectangles.

The Fermi contact hyperfine parameter, A_0, depends linearly on the spin density at the nucleus, $\rho_{\text{spin}}(0)$ [Eq. (2)]. Data presented in Figs. 6 and 7 show that there are strong correlations between $\rho_{\text{spin}}(0)$ and average bond angle and average bond length around a defect DB. The mean Si-Si-Si bond angle for P_{b0} DB atoms in Table I ranges from 110 to 120°. As the average bond angle at the DB atom tends to 120°, the hybridization at the DB atom tends to sp^2 and $\rho_{\text{spin}}(0)$ tends to zero because the DB state is purely $3p$ in character. The variation of the A_0 parameter with average bond length to the P_{b0} DB atom is also shown in Fig. 6. There is a clear trend in the value of the A_0 parameter with bond length also. The number of P_{b0} defects found in this paper (three in 12 interfaces in the six supercells studied) is surprisingly small. The experimental value of the Fermi contact (around 10 mT) implies a mean Si-Si-Si bond angle of around 108° (close to the tetrahedral angle) while the three defects found in this paper had higher mean bond angles and consequently lower Fermi contact parameters. Two of the P_{b0} defects found had hyperfine axes close to the [111] direction and one was 37.7° from the [111] direction. The small number of P_{b0} defects found does not permit any conclusions regarding statistics of these defects to be drawn.

Six P_{b1} defects were identified among the 12 interfaces generated. Two of these were in a positively charged state according to the atom electron population for the primary defect atom. These defects had magnetic moments of 0.03 and 0.06 μ_B. The remaining four defects were in a neutral, spin-polarized state with magnetic moments between 0.39 and 0.61 μ_B on the primary defect atom (Table II). Each of the cells generated in this paper contained more than one defect type in a range of local environments. Each defect can exist in more than one charge state and it is therefore possible to find a particular defect in more than one charge state in different local environments. The spin density on defect 1 in Table II is shown in Fig. 4(b). The atom projected density of states for the neutral P_{b1} defects in Fig. 5 shows a similar density of states to that for the P_{b0} defects, with a slightly larger exchange splitting. Mean bond angles to the central defect atom range from 103 to 113° (Fig. 6).

TABLE I. Hyperfine parameters of P_{b0} defects. The fraction of the magnetic moment localized on the DB atom (μ_B), the angle made by the principal axis of the hyperfine tensor with the [111] direction, and Fermi contact and principal components of the anisotropic hyperfine tensor (mT) are given.

Defect	Moment μ_B	Axis	a	b	A_1^1	A_1^2	A_1^3
1	0.66	9.2°	5.7	2.0	3.9	−2.0	−1.9
2	0.47	37.7°	9.2	1.4	2.7	−1.4	−1.3
3	0.49	3.7°	1.9	1.7	3.3	−1.7	−1.6
Expt. [3]			10.0–10.7	2.2			

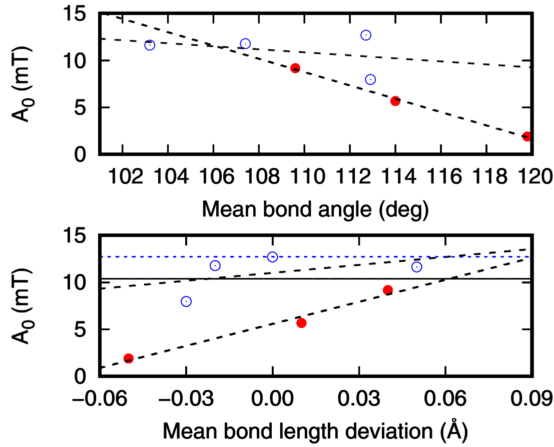

FIG. 6. Variation of A_0 hyperfine tensors of P_b defects with mean bond angle and with deviation from the mean bond length for a particular defect type. Solid red circles, P_{b0} defects; hollow blue circles, P_{b1} defects. Linear regression fits are shown for each defect type. Experimental hyperfine parameters for P_{b0} and P_{b1} defects are indicated by horizontal solid and dotted lines.

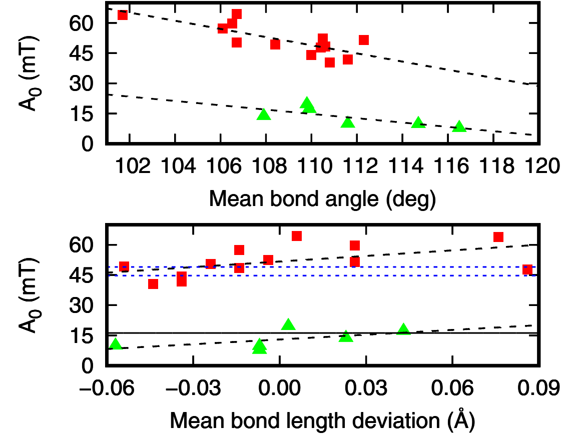

FIG. 7. Variation of the isotropic Fermi contact part of hyperfine tensors for E' and $(Si_2O)Si\cdot$ P_b defects with mean bond angle and with the deviation from the mean bond length for a particular defect type. Red squares are E' defects in the a-SiO_2 layer and green triangles are $(Si_2O)Si\cdot$ P_b defects. Linear regression fits are shown for each defect type. Experimental hyperfine parameters for E'_α, E'_γ, and the S resonance at 16.2 mT are shown as horizontal dotted and solid lines.

Principal axis directions for all of the neutral defects lie approximately 20° from the [001] direction. Values obtained from experiment (32.3°) [4] are close to the [112] direction (35.3°). A previous DFT calculation [26] considered dimer and asymmetrically oxidized dimer (AOD) models for the P_{b1} defect (Table II). The tilt angle and a and b parameters for the dimer model are in good agreement with parameters for the dimer structures found in this paper, but all have a lower tilt angle (around 20°) than found in experiment (32.3°). The AOD model has a tilt angle (30°) in agreement with experiment, as the Si dimer bond is tilted in that case, although the axial hyperfine parameter (a = 15.5 mT) is not in as good agreement with experiment (a = 12.7 mT) as the dimer structure. Principal components of the $\mathbf{A}_1$ tensors for the defects in Table II show that the P_{b1} defect is close to axial symmetry.

C. $Si_2O{\equiv}Si\cdot$ defects

Atomic structures of clean, ordered Si(001) surfaces consist of ordered Si dimers. Si(001)/a-SiO_2 interfaces in this paper, which were generated using unoxidized Si layers, were dimerized to a large extent after relaxation using PBE DFT. Dimers at clean Si(001) surfaces have two DBs which have a spin paired, singlet ground state. DBs in an interface dimer form bonds to O or Si atoms in the oxide layer. At clean, dimerized Si(001) surfaces, dimers form rows which run perpendicular to the dimer bond. In the (2 × 2) supercells used in this paper, an ordered dimer network similar to those at clean surfaces can form. However, formation of the a-SiO_2 interface can also lead to dimer mismatch. A defect free, clean Si(001) surface is formed when rows of Si atoms in the topmost bilayer displace from their crystal lattice sites in a correlated way in order to form parallel rows of Si dimers. When Si dimers form at the Si(001)/a-SiO_2 interface, the topmost rows of Si atoms must displace in a similar way. However, the proximity of atoms in the a-SiO_2 may prevent these parallel rows from forming and result in a new kind of interface defect. This is a defect in which Si atoms in the topmost Si layer are available to form a Si dimer but the partner Si atom has been displaced in the "wrong" sense and forms a Si dimer bond with a Si atom in another row. This type of dimer mismatch will be eliminated by thermal fluctuations at a clean Si(001) surface but may be retained at a Si(001)/a-SiO_2 interface because strong bonds are formed between topmost Si layer atoms and atoms in the amorphous oxide layer. The presence of relatively abundant

TABLE II. Hyperfine parameters of P_{b1} defects. The fraction of the magnetic moment localized on the DB atom (μ_B), the angle made by the principal axis of the hyperfine tensor with the [001] direction, and Fermi contact and principal components of the anisotropic hyperfine tensor (mT) are given.

Defect	Moment μ_B	Axis	a	b	A_1^1	A_1^2	A_1^3
1	0.61	16.3°	11.8	1.8	3.6	−1.8	−1.7
2	0.57	19.9°	12.7	1.7	3.4	−1.7	−1.7
3	0.55	21.6°	8.0	1.7	3.5	−1.8	−1.7
4	0.39	18.2°	11.6	1.2	2.4	−1.2	−1.2
Expt. [4]		32.3°	12.7	2.0			
DFT dimer [26]		21°	12.6	1.5			
DFT oxidized dimer [26]		30°	15.5	1.6			

TABLE III. Hyperfine parameters of $Si_2O{\equiv}Si\cdot$ defects. The fraction of the magnetic moment localized on the DB atom (μ_B), the angle made by the principal axis of the hyperfine tensor with the [111] direction, and Fermi contact and principal components of the anisotropic hyperfine tensor (mT) are given.

Defect	Moment μ_B	Axis	a	b	A_1^1	A_1^2	A_1^3
1	0.61	43.9°	19.5	1.8	3.7	−1.9	−1.8
2	0.60	41.4°	17.2	1.7	3.5	−1.8	−1.7
3	0.54	30.7°	9.7	1.6	3.3	−1.7	−1.6
4	0.51	28.0°	9.9	1.7	3.3	−1.7	−1.6
5	0.48	32.2°	13.6	1.3	2.7	−1.4	−1.3
6	0.27	11.0°	7.7	1.5	3.0	−1.6	−1.4

P_{b1} defects at the interface implies the existence of Si dimer bonds at the interface since they are unsaturated Si dimers with dangling electrons. In the present paper, provided that Si dimer formation is not inhibited by insertion of O dimer bridges, there is a strong tendency for Si dimers to form during DFT energy minimization. If Si dimers exist on the clean Si(001) surface before oxidation, which seems likely, formation of P_{b1} defects may occur by attachment of an O atom to one of the Si dimer atoms. Cleavage of Si dimer bonds during oxidation could result in formation of a dimer mismatch defect. Defects of this type, in which the surface Si atom with the DB is bonded to two Si atoms in the Si bulk layer below and one O atom in the oxide layer above, are denoted $Si_2O{\equiv}Si\cdot$ defects. Six defects of this kind were found in these calculations and their A_0 parameters are given in Table III.

Examples of $Si_2O{\equiv}Si\cdot$ defects are shown in Figs. 4(c) and 4(d). Two Si dimers in Fig. 4(c) are marked 1 and 2. Instead of occurring in one dimer row they occur in adjacent rows. The right Si atom in dimer 1 could have formed a dimer with the DB the spin density of which is shown, but it has been displaced in the opposite sense, leaving one DB and a dimer mismatch. Periodic boundary conditions used do not prevent the Si atom with the DB from forming a dimer with its neighbor to the right, but the a-SiO_2 structure at the interface may prevent this. In a second $Si_2O{\equiv}Si\cdot$ defect in Fig. 4(d), a DB which is oriented to form a dimer is instead directed towards an O atom.

The atom projected DOS for $Si_2O{\equiv}Si\cdot$ dimers in Fig. 5 shows that the occupied states are deeper in energy than P_{b0} and P_{b1} $Si_3{\equiv}Si\cdot$ defects. The hyperfine A_0 parameter ranges from 7.7 to 19.5 mT. The variation of this parameter with average bond angle and deviation from the average of all bond lengths to these defect atoms is shown in Fig. 7. The lowest values of A_0 occur for the largest bond angles, i.e., as the hybridization approaches sp^2 hybridization. The hyperfine tensors for these defects are nearly axial and variation in the angle made with [111] directions is large. Properties of these defects (intermediate hyperfine A_0 values, large variation in principal axis orientation, occurrence at the Si/a-SiO_2 interface) make it a possible candidate for the origin of an ESR resonance denoted S [9]. It is characterized by a broad resonance for which it has been difficult to find features which might be identified as ^{29}Si hyperfine coupling and it is known to exist in a layer which is sharply confined to the Si/a-SiO_2 interface.

D. E' defects

Defects in α quartz [61] and a-SiO_2 are denoted E' [62–64]. Defects denoted E'_α [37–39], E'_β [37], E'_γ [40–43], and E'_δ [37,44,45] have been identified by ESR in a-SiO_2. Creation of E' defects in a-SiO_2 by UV radiation has been attributed to dissociation of Si-H bonds in both experimental [65] and computational [66] studies. An experimental study of the ^{29}Si hyperfine structure of a-SiO_2 found two ESR doublets with splittings of 42 and 49 mT with a full width at half maximum of 4.5 mT for the 49-mT peak [39]. These were assigned to E'_γ and E'_α defects [39]. Values of hyperfine parameters for E' defects are E'_α (49 mT [39]), E'_γ (42 mT [39,40]), and E'_δ (10 mT [45,67]). On the basis of comparison of measured and predicted ESR hyperfine parameters, E'_α defects have been assigned to defect structures in which the Si DB spin interacts with a neighboring O atom [68,69]. E'_γ defects have been assigned to puckered or unpuckered Si DB [68–70] and a bridged hole-trapping oxygen deficiency center [71]. The main distinction between E'_α and E'_γ defects, which have similar hyperfine parameters, may be interaction of the Si DB spin with a nearby O atom. E'_δ defects are characterized by a hyperfine parameter of 10 mT and an intensity ratio of the hyperfine multiplet to the main ESR signal of 20.3 ± 1.9%, which indicates that the spin observed in ESR is delocalized over four Si atoms [67]. E'_δ defects have been assigned to positively charged, long Si-Si bonds containing one spin [70]. In this case the DB spin is mainly localized on one Si atom, not four. Furthermore, the predicted g tensor for the positively charged Si dimer bond is anisotropic and overestimates experimental values [69]. Experimental evidence [45,67] therefore contradicts an assignment of the E'_δ signal to a positively charged long Si-Si bond.

Most theoretical studies of E' defects in a-SiO_2 generate them by removing [43,69–71] or displacing [38] an O atom and relaxing the system in one or more charge and spin states. As noted above, in this paper E' defects form when a-SiO_2 is placed onto c-Si and the system is relaxed. The most common E' configuration which results from this approach to structure generation is the forward projected structure [69] in which the Si DB atom is directed towards an O atom (which is bonded to other Si atoms) and the Si-O distance ranges from 2.0 to 3.8 Å. In extreme cases the Si-O distance is as low as 2 Å and this results in a hyperfine parameter over 60 mT. Two defects were found in which the forward projected Si DB is directed towards a doubly bonded (silanone) oxygen. Hyperfine parameters for these E' defects are 64.4 and 67.5 mT. In other cases the Si-O distance is 2.9 Å and the hyperfine parameter is 40 mT, close to the experimental value for an E'_γ defect [39]. More commonly the Si-O distance is around 2.5 Å and the hyperfine parameter is around 50 mT, similar to the parameter assigned to the E'_α defect [39]. Correlations between hyperfine parameters of E' defects and mean bond angle or bond length deviation are shown in Fig. 7. The experimentally observed hyperfine splittings of 42 and 49 mT are shown as a pair of dotted blue lines in the figure. Our computed values cluster around these

values, with the exception of a small number of defects with unusual geometries and high hyperfine constants.

IV. DISCUSSION

We have presented simulations of the Si(001)/a-SiO_2 interface using a combination of CFF-MD and first-principles structure relaxation calculations. Interface atomic structures were generated by taking a layer of a-SiO_2 and placing it on top of a (001) terminated bulk Si layer. The combined a-SiO_2 and bulk Si cell was equilibrated using CFF-MD before being relaxed using a DFT total-energy minimization method. The protocol results in a linear defect density that is about ten times higher than experimentally determined defect densities at the Si(001)/a-SiO_2 interface and for E' defects in a-SiO_2, yielding correspondingly higher areal and volume densities. The defects which form are mainly those expected from published experimental and simulation work, including P_{b0} and P_{b1} DB defects and E' bulk a-SiO_2 defects. An additional Si DB defect is generated in this paper which results from a Si dimer mismatch.

The COMB10 potential used in this paper does not predict formation of Si dimers at the Si surface. When the equilibrated interface obtained using the COMB10 CFF-MD is relaxed using DFT, there is a strong tendency for Si dimers to form unless O atoms are deliberately inserted between the outermost Si atoms in the bulk Si layer. The reliability of the COMB10 potential for reproducing structures and energetics of small Si_xO_y clusters with low atomic coordination number has been questioned and a bug in the LAMMPS implementation of the potential was corrected in a December 2013 release [72]. The inability of COMB10 to reproduce Si dimerization predicted by subsequent DFT relaxation is therefore not unexpected. However, the amorphous structures generated by high-temperature annealing and quenching using the COMB10 potential are expected to be reasonable representations of the structure of a-SiO_2. The version of LAMMPS used in this paper was released in September 2014 and is therefore not affected by the bug corrected in 2013. The authors of Ref. [33] used the ReaxFF force field [34] to anneal a-SiO_2 in contact with a Si(001) layer with its atomic positions fixed during the anneal. They found that O diffused from the a-SiO_2 layer to interstitial sites in the Si(001) layer during the anneal. Hence, further improvements in protocols for generating realistic semiconductor/amorphous oxide interfaces and CFF which can accurately reproduce oxidation kinetics at interfaces are required.

The question of dimer formation at the Si(001)/a-SiO_2 interface has been considered before [73]. The presence of P_{b1} defects at the interface which have been assigned to Si dimers with a DB implies that the surface is indeed dimerized. Stesmans and coworkers [4] report a P_{b1} density of up to 7×10^{12} cm^{-2} (2% of a 2×1 monolayer), which compares to the dimer density at clean Si(001) surfaces of 3×10^{14} cm^{-2}. Considering that some P_{b1} defects are charged and therefore not seen in ESR and that a fraction of surface dimers will have a DB, the extent of Si dimer formation at the interface may be quite high (say, several tenths of a monolayer). Si dimers might be expected to be observed in Si $2p_{3/2}$ photoemission experiments since this line is shifted to lower binding energy by 0.5 eV for dimers at the clean Si(001) surface [17]. Interface dimers do produce a weak feature to the low-binding-energy side of the DOS in our interface calculations, but this is barely distinguishable in the curve shown in Fig. 3.

Defect DOSs for P_b and $Si_2O{\equiv}Si\cdot$ in Fig. 5 show spin splitting and Fermi levels around mid-band-gap. Estimates of interface state densities for this system have been made using spectroscopic CP experiments [15], DLTS [14], and ESR [13]. CP and ESR show double peaked defect densities for P_b defects similar to those referred to in Fig. 5. Campbell and Lenahan [13] argue for a broad double peaked DOS for P_{b0} and a much narrower double peaked DOS for P_{b1}. Given the similarity of the two defects it is difficult to explain such a difference. The double peaked DOS found by CP was attributed to amphoteric P_b defects which can exist in +1, neutral, or −1 charge states, which is in agreement with the results of this paper. Fermi levels which result in the charge neutral cells in this paper result in P_b defects of both kinds which are in neutral or −1 charge states. Results of DLTS experiments are consistent with an occupied defect level 0.3 eV below the bulk conduction band edge. This was attributed to P_b defects [14].

A defect denoted S has been observed at the a-SiO_2 surface and a-SiO_2/Si(001) interface of an a-SiO_2 film grown on Si(001). It can occur with high areal density (up to 10^{15} cm^{-2} after annealing at 1250 °C for 1 h [9]). It was postulated to be either an $Si_2O{\equiv}Si\cdot$ or an $SiO_2{\equiv}Si\cdot$ defect given its hyperfine splittings of 16.2 and 28.8 mT. Hydrogen fluoride etch measurements show that the S defect was localized within 40 Å of the a-SiO_2 surface and the a-SiO_2/Si(001) interface. The measured thickness could be limited by the resolution of the experiment, so that the defect is actually more localized at the surface and interface than this value indicates. The hyperfine splitting of Si DB defects increases with the number of O ions bonded to the DB Si atom. The value of 16.2 mT is characteristic of an $Si_2O{\equiv}Si\cdot$ defect (Fig. 7 and Table III). Since there are S defects with a likely $Si_2O{\equiv}Si\cdot$ stoichiometry localized at the a-SiO_2/Si(001) interface in the work of Stesmans *et al.* [9], these may be the mismatched dimer defects found in this paper.

The a-SiO_2 layer which is placed on top of a Si(001) slab is generated in a cell with periodic boundary conditions. The DOS in Fig. 1 (middle panel) shows no states in the band gap. When this is placed on the 2×2 Si(001) layer and the cell contents and cell parameters are allowed to relax, there are between one and four E' defects in the six interface cells used in this paper. It is likely that stress during structure relaxation leads to Si-O bond breaking and E' defect formation. An extensive nomenclature (puckered, unpuckered, back-projected, forward oriented, etc.) has been developed for E' defects in SiO_2 and a-SiO_2, especially in describing how the lattice relaxes when O vacancies are created by removing an O atom in a simulation [69,70]. Defects which form in the a-SiO_2 layer in this paper are almost all of the kind shown in Fig. 4(e) where the DB is directed towards a single O atom or (as in Fig. 4) between two O atoms. This type of defect is denoted forward oriented by Giacomazzi *et al.* [69] and it probably forms because the a-SiO_2 is stressed when it is relaxed on top of the Si layer. The distance between the DB Si atom and the nearest O neighbor is in the range 2.3 to 3.1 Å. There is

TABLE IV. Hyperfine parameters of E' defects. The fraction of the magnetic moment localized on the DB atom (μ_B) and Fermi contact and principal components of the anisotropic hyperfine tensor (mT) are given.

Defect	Moment μ_B	a	b	A_1^1	A_1^2	A_1^3
1	0.83	64.4	1.6	3.2	−1.6	−1.6
2	0.65	52.3	1.2	2.5	−1.3	−1.2
3	0.90	49.3	1.8	3.6	−1.7	−1.8
4	0.73	40.5	1.8	3.7	−1.9	−1.8

an inverse correlation between distance and Fermi hyperfine constants. This may be because the spin density is localized on the parent Si atom by the proximity of a closed-shell O atom. The largest hyperfine parameters in Table IV and Fig. 7 are for a defect which has the E' DB close to a silanone O atom.

In other simulation work [26,32] defects at the Si(001)/a-SiO_2 interface were generated using relaxed structures with continuous random networks (i.e., with no defects) and defects were generated by removing one O atom. Defects generated in this way are sometimes studied with supercells which are either charge neutral or in a positively charged state [43,69,70] in order to gain additional information about alternative charge states of the defect. In the present paper there are relatively large numbers of defects per supercell and only neutral supercells were studied. In this case the Fermi level for the neutral cell determines the overall charge state of each defect. Giving the supercell a positive charge will change the charge state of one of these defects. CFF-MD calculations [38] have shown that simply displacing an O atom in a fully coordinated α quartz cell (mimicking the effect of irradiation) can result in formation of a pair of E' defects with single dangling electrons after structure relaxation without positively charging the cell. Hence E' defects which are presented in simulation work depend on the method used to generate them. Simulation methods which can accurately reproduce chemical potentials and interatomic force fields between elements present at the interface are needed for more realistic simulations. The COMB10 potential fails to reproduce Si dimerization at the a-SiO_2/Si(001) interface in disagreement with further DFT structure relaxation.

V. SUMMARY AND CONCLUSIONS

DFT calculations on six supercells with periodic boundary conditions containing a-SiO_2 and Si(001) layers were used to study defects which form at the a-SiO_2/Si(001) interface and to obtain their hyperfine tensors and defect valence and Si $2p$ DOS. Structures were generated by placing an a-SiO_2 layer on a bulk terminated Si(001) layer (with or without surface O atoms). Structures were fully relaxed using a PBE DFT Hamiltonian. DOS and hyperfine parameters were calculated using a hybrid DFT method, which predicts the correct electronic band gap for bulk c-Si. The linear density of interface and bulk a-SiO_2 defects is about ten times higher than found in experiment. An alternative approach in simulation of interface systems is to use a defect free, continuous random network and generate a defect by removing an O atom. The method adopted here produces the P_{b0} and P_{b1} defects previously identified by ESR experiments as well as $Si_2O{\equiv}Si\cdot$ defects which result from Si dimer mismatches in the dimer formation process which leave $Si_2O{\equiv}Si\cdot$ DBs oriented parallel to the interface. a-SiO_2 generated by annealing α quartz to high temperature in a CFF-MD run has no states in the electronic band gap. "Forward oriented" E' defects are the most common defect found in the bulk a-SiO_2 after it has been placed between two Si(001) layers and the system has fully relaxed. No bulk defects with low hyperfine A_0 parameters are found, which might be the E'_δ defect in a-SiO_2. Interfaces where the Si(001) layer had a perfect bulk termination before relaxation had a strong tendency to form Si dimers. Adding O atoms between rows of Si atoms in outer layers in a 2×1 periodicity prevents dimers from forming when the structure was relaxed in a DFT calculation. Experimental observation of up to 2% P_{b1} defects (which are Si dimers with a DB) is believed to be evidence for a tendency for Si dimers to form at the a-SiO_2/Si(001) interface.

ACKNOWLEDGMENTS

E.M. acknowledges the support of the Irish Higher Education Authority through the Progress in Research in Third Level Institutes (PRTLI)-V program. All calculations were performed on the Kelvin and Fionn clusters maintained by the Trinity Centre for High Performance Computing and the Irish Centre for High End Computing, respectively. The Kelvin cluster was funded through grants from the Irish Higher Education Authority, through its PRTLI program.

APPENDIX: COMPUTATIONAL DETAILS

The LAMMPS CFF-MD code [47] was used to generate a-SiO_2 atomic positions in a cell with dimensions fixed at $10.82 \times 10.82 \times 10.82$ Å in a high-temperature run at 5000 K followed by rapid cooling to 200 K using a Nosé-Hoover thermostat in an NPT ensemble and the COMB10 CFF [16].

DFT relaxation steps using the CASTEP code [50] and the PBE exchange-correlation functional [49] were continued until forces on atoms were less than 2×10^{-4} eV/Å. Calculations with CASTEP used the Si 00 PBE OP and O 00 PBE OP OPIUM family of pseudopotentials for Si and O available in CASTEP with the CASTEP "precise" cutoff energy (900 eV in this case). We used $4 \times 4 \times 4$ and $4 \times 4 \times 2$ Monkhorst-Pack meshes [74] for a-SiO_2 and a-SiO_2/Si(001) supercells, respectively.

Hybrid DFT calculations were performed using the CRYSTAL program [52] and a modified B3LYP functional described in Ref. [51]. The all-electron basis sets used for Si and O are described in Refs. [75] and [76]. A $2 \times 2 \times 2$ Monkhorst-Pack mesh was used for CRYSTAL calculations.

Density of states calculations were performed using the EXCITON code [53] using wave functions and energy eigenvalues from hybrid DFT calculations using CRYSTAL.

[1] M. Masuduzzaman, B. Weir, and M. A. Alam, J. Appl. Phys. **111**, 074501 (2012).
[2] D. Veksler, G. Bersuker, A. Koudymov, and M. Liehr, IEEE Trans. Electron Devices **60**, 1514 (2013).
[3] H. J. von Bardeleben and J. L. Cantin, Braz. J. Phys. **27**, 314 (1997).
[4] A. Stesmans, B. Nouwen, and V. V. Afanas'ev, Phys. Rev. B **58**, 15801 (1998).
[5] A. Stesmans and V. V. Afanas'ev, J. Phys.: Condens. Matter **10**, L19 (1998).
[6] P. M. Lenahan and J. F. Conley, J. Vac. Sci. Technol. B **16**, 2134 (1998).
[7] K. Keunen, A. Stesmans, and V. V. Afanas'ev, Phys. Rev. B **84**, 085329 (2011).
[8] T. Matsuoka, L. S. Vlasenko, M. P. Vlasenko, T. Sekiguchi, and K. M. Itoh, Appl. Phys. Lett. **100**, 152107 (2012).
[9] A. Stesmans, B. Nouwen, and V. V. Afanas'ev, Phys. Rev. B **66**, 045307 (2002).
[10] T. D. Mishima, P. M. Lenahan, and W. Weber, Appl. Phys. Lett. **76**, 3771 (2000).
[11] A. Stesmans and V. V. Afanas'ev, Appl. Phys. Lett. **78**, 1451 (2001).
[12] T. D. Mishima, P. M. Lenahan, and W. Weber, Appl. Phys. Lett. **78**, 1453 (2001).
[13] J. P. Campbell and P. M. Lenahan, Appl. Phys. Lett. **80**, 1945 (2002).
[14] L. Dobaczewski, S. Bernardini, P. Kruszewski, P. K. Hurley, V. P. M. abd I. D. Hawkins, and A. R. Peaker, Appl. Phys. Lett. **92**, 242104 (2008).
[15] J. T. Ryan, L. C. Yu, J. H. Han, J. J. Kopanski, K. P. Cheung, F. Zhang, C. Wang, J. P. Campbell, and J. S. Suehle, Appl. Phys. Lett. **98**, 233502 (2011).
[16] T. R. Shan, B. D. Devine, J. M. Hawkins, A. Asthagiri, S. R. Phillpot, and S. B. Sinnott, Phys. Rev. B **82**, 235302 (2010).
[17] F. J. Himpsel, F. R. McFeely, A. Taleb-Ibrahimi, J. A. Yarmoff, and G. Hollinger, Phys. Rev. B **38**, 6084 (1988).
[18] Z. H. Lu, D. T. J. M. J. Graham and, and K. H. Tan, Appl. Phys. Lett. **63**, 2941 (1993).
[19] S. D. Kosowsky, P. S. Pershan, K. S. Krisch, J. Bevk, M. L. Green, D. Brasen, L. C. Feldman, and P. K. Roy, Appl. Phys. Lett. **70**, 3119 (1997).
[20] J. H. Oh, H. W. Yeom, Y. Hagimoto, K. Ono, M. Oshima, N. Hirashita, M. Nywa, A. Toriumi, and A. Kakizaki, Phys. Rev. B **63**, 205310 (2001).
[21] A. Bongiorno, A. Pasquarello, M. S. Hybertsen, and L. C. Feldman, Phys. Rev. Lett. **90**, 186101 (2003).
[22] I. Ohdomari, H. Akatsu, Y. Yamakoshi, and K. Kishimoto, J. Non-Cryst. Solids **89**, 239 (1987).
[23] J. Yu, S. B. Sinnott, and S. R. Phillpot, Phys. Rev. B **75**, 085311 (2007).
[24] G. Kovačević and B. Pivac, J. Appl. Phys. **115**, 043531 (2014).
[25] A. Pasquarello, M. S. Hybertsen, and R. Car, Nature (London) **396**, 58 (1998).
[26] A. Stirling, A. Pasquarello, J.-C. Charlier, and R. Car, Phys. Rev. Lett. **85**, 2773 (2000).
[27] T. Yamasaki, C. Kaneta, T. Uchiyama, T. Uda, and K. Terakura, Phys. Rev. B **63**, 115314 (2001).
[28] T. Yamasaki, K. Kato, and T. Uda, Phys. Rev. Lett. **91**, 146102 (2003).
[29] K. Kato, T. Yamasaki, and T. Uda, Phys. Rev. B **73**, 073302 (2006).
[30] S. Markov, P. Sushko, C. Fienga, E. Sangiorgi, A. Shluger, and A. Asenov, J. Phys. Conf. Ser. **242**, 012010 (2010).
[31] K. O. Ng and D. Vanderbilt, Phys. Rev. B **59**, 10132 (1999).
[32] F. Giustino, A. Bongiorno, and A. Pasquarello, J. Phys.: Condens. Matter **17**, S2065 (2005).
[33] L. Gerrer, S. Ling, S. M. Amoroso, P. Asenov, A. L. Shluger, and A. Asenov, J. Comput. Electron. **12**, 638 (2013).
[34] A. C. T. van Duin, S. Dasgupta, F. Lorant, and W. A. Goddard, J. Phys. Chem. A **105**, 9396 (2001).
[35] R. Buczko, S. J. Pennycook, and S. T. Pantelides, Phys. Rev. Lett. **84**, 943 (2000).
[36] D. L. Griscom, E. J. Friebele, K. J. Long, and J. W. Fleming, J. Appl. Phys. **54**, 3743 (1983).
[37] D. L. Griscom, Nucl. Instrum. Meth. Phys. Res., Sect. B **1**, 481 (1984).
[38] M. Boero, A. Oshiyama, and P. L. Silvestrelli, Phys. Rev. Lett. **91**, 206401 (2003).
[39] G. Buscarino, S. Agnello, and F. M. Gelardi, Phys. Rev. Lett. **97**, 135502 (2006).
[40] D. L. Griscom, Phys. Rev. B **20**, 1823 (1979).
[41] M. Boero, A. Pasquarello, J. Sarnthein, and R. Car, Phys. Rev. Lett. **78**, 887 (1997).
[42] P. E. Blöchl, Phys. Rev. B **62**, 6158 (2000).
[43] A. Stirling and A. Pasquarello, Phys. Rev. B **66**, 245201 (2002).
[44] D. L. Griscom and E. J. Friebele, Phys. Rev. B **34**, 7524 (1986).
[45] G. Buscarino, S. Agnello, and F. M. Gelardi, Phys. Rev. Lett. **94**, 125501 (2005).
[46] A. Stesmans, K. Clémer, and V. V. Afanas'ev, Phys. Rev. B **77**, 094130 (2008).
[47] S. Plimpton, J. Comp. Phys. **117**, 1 (1995).
[48] See http://www.lammps.sandia.gov.
[49] J. P. Perdew, K. Burke, and M. Ernzerhof, Phys. Rev. Lett. **77**, 3865 (1996).
[50] S. J. Clark, M. D. Segall, C. J. Pickard, P. J. Hasnip, M. I. J. Probert, K. Refson, and M. C. Payne, Zeitschrift für Kristallographie - Crystalline Materials **220**, 567 (2005).
[51] S. Banerjee, J. F. McGilp, and C. H. Patterson, Phys. Status Solidi B **252**, 78 (2015).
[52] R. Dovesi, V. R. Saunders, C. Roetti, R. Orlando, C. M. Zicovich-Wilson, F. Pascale, B. Civalleri, K. Doll, N. M. Harrison, I. Bush *et al.*, CRYSTAL09 User's Manual, University of Torino, Torino, 2009.
[53] C. H. Patterson, Mol. Phys. **108**, 3181 (2010).
[54] G. A. Lager, J. D. Jorgensen, and F. J. Rotella, J. Appl. Phys. **53**, 6751 (1982).
[55] L. A. J. Garvie, P. Rez, J. R. Alvarez, P. R. Buseck, A. J. Craven, and R. Brydson, Am. Mineral. **85**, 732 (2000).
[56] Z. A. Weinberg, G. W. Rubloff, and E. Bassous, Phys. Rev. B **19**, 3107 (1979).
[57] K. Vollmayr, W. Kob, and K. Binder, Phys. Rev. B **54**, 15808 (1996).
[58] See Supplemental Material at http://link.aps.org/supplemental/10.1103/PhysRevMaterials.1.044602 for the structure of the 84 atom *a*-SiO_2 unit cell generated in a classical force field molecular dynamics run at 5000 K and structures of the six *a*-SiO_2/Si(001) supercells used in this work, as well as radial distribution functions for both systems.

[59] G. Mallia, R. Orlando, C. Roetti, P. Ugliengo, and R. Dovesi, Phys. Rev. B **63**, 235102 (2001).
[60] A. Stesmans, Phys. Rev. B **48**, 2418 (1993).
[61] C. J. Pickard and F. Mauri, Phys. Rev. Lett. **88**, 086403 (2002).
[62] J. A. Weil, Phys. Chem. Miner. **10**, 149 (1984).
[63] M. G. Jani, R. B. Bossoli, and L. E. Halliburton, Phys. Rev. B **27**, 2285 (1983).
[64] R. I. Mashkovtsev and Y. Pan, Phys. Chem. Miner. **39**, 79 (2012).
[65] V. V. Afanas'ev and A. Stesmans, J. Phys.: Condens. Matter **12**, 2285 (2000).
[66] S. Ling, A. El-Sayed, F. Lopez-Gejo, M. B. Watkins, V. Afanas'ev, and A. L. Shluger, Microelectron. Eng. **109**, 310 (2013).
[67] M. Jivanescu, A. Stesmans, and V. V. Afanas'ev, Phys. Rev. B **83**, 094118 (2011).
[68] G. Buscarino, R. Boscaino, S. Agnello, and F. M. Gelardi, Phys. Rev. B **77**, 155214 (2008).
[69] L. Giacomazzi, L. Martin-Samos, A. Boukenter, Y. Ouerdane, S. Girard, and N. Richard, Phys. Rev. B **90**, 014108 (2014).
[70] S. Mukhopadhyay, P. V. Sushko, A. M. Stoneham, and A. L. Shluger, Phys. Rev. B **70**, 195203 (2004).
[71] T. Uchino and T. Yoko, Phys. Rev. B **74**, 125203 (2006).
[72] T. Hynninen, T. Musso, and A. S. Foster, Modell. Simul. Mater. Sci. Eng. **24**, 035022 (2016).
[73] F. Rochet, C. Poncey, G. Dufour, H. Roulet, C. Guillot, and F. Sirotti, J. Non-Cryst. Solids **216**, 148 (1997).
[74] H. Monkhorst and J. D. Pack, Phys. Rev. B **13**, 5188 (1976).
[75] F. Pascale, M. Catti, A. Damin, R. Orlando, V. Saunders, and R. Dovesi, J. Phys. Chem. B **109**, 18522 (2005).
[76] M. D. Towler, N. L. Allan, N. M. Harrison, V. R. Saunders, W. C. Mackrodt, and E. Aprà, Phys. Rev. B **50**, 5041 (1994).